Efficiency Analysis of Canards-Based Course Correction Fuze for a 155-mm Spin-Stabilized Projectile

Eric Gagnon[1] and Alexandre Vachon[2]

Abstract: There are many course correction fuze concepts for improving the precision of a spin-stabilized projectile. Some of them consist in a despun fuze equipped with canards. Canards provide continuous and, possibly, modulable maneuvering capabilities in crossrange and downrange. This paper analyzes the efficiency of this type of course correction fuze and determines the best configuration for the canards. To do so, four concepts of canards-based course correction fuze are proposed and tested. To properly operate the fuzes, a guidance algorithm, based on point-of-impact prediction, and two autopilots, a poles/zeros cancellation controller and a proportional integrator controller, are developed. The fuzes efficiency is studied with their control authority footprint and achieved performances during Monte-Carlo simulations. All the tests are done with a pseudo-seven-degrees-of-freedom simulator including the developed algorithms. Those tests demonstrate that the four concepts significantly improve the precision of a spin-stabilized projectile and that, with the proposed algorithms, the best precision is obtained when the canards directly handle the projectile longitudinal acceleration. **DOI: 10.1061/(ASCE)AS.1943-5525.0000634.**

Introduction

In recent years, the mission of artillery has evolved from fire support, where relatively large dispersion is allowed, to precise fire. Specially developed precision-guided munitions succeed quite well at this new task. However, these specific designs represent high-cost options. An alternative strategy is to develop course correction fuzes (CCF) for existing conventional shells to give maneuvering capabilities to otherwise unguided projectiles.

The major dispersion of unguided projectiles being in the downrange direction, some concepts of CCF are oriented to make trajectory corrections along the longitudinal axis. These concepts (Hollis and Brandon 1999; Kautzsch and Reusch 2003) use drag brakes, deployable surfaces which decrease projectile velocity and range. Crossrange corrections can be achieved by spin brakes, devices that decrease the projectile spin rate (Hillstrom and Osborne 2005). However, these spin brake concepts yield only small capabilities (Grignon et al. 2007). Also, actual drag and spin brakes are single shot deployable control surfaces. Therefore, with these devices, it is impossible to increase neither the range nor the drift and to compensate for perturbations occurring late in the flight.

An alternative existing CCF concept, providing downrange and crossrange corrections, consists in a roll-decoupled fins ring equipped with canards. Even if it has been demonstrated (Ollerenshaw and Costello 2008) that, for a spin-stabilized projectile, the ideal location for control surfaces is the projectile tail, the concept of canards-based course correction fuze (CCCF) is still widely studied. It appeared in the 1970s (Reagan and Smith 1975) and, with the evolution and miniaturization of relevant technologies, has regained interest lately [J. A. Clancy et al., "Fixed canard 2-d guidance of artillery projectiles," U.S. Patent No. 6,981,672 B2 (2006); Wernert et al. 2008; Bybee 2010]. It has been demonstrated (Gagnon and Lauzon 2008) that, even if it is less efficient than continuous feedback control concept combining drag brake and spin brake, roll-decoupled CCCF is an efficient way to increase projectile precision. Also, in opposition to drag and spin brakes, CCCF provides continuous control, allowing accounting for disturbances occurring late in the flight. Furthermore, the canards can be actuated in order to provide scalable forces when the predicted miss does not require large corrections. However, a force perpendicular to the spin axis of a spin-stabillized projectile and applied in front of its center of mass, like canards generate, results in out-of-plane swerve motion (Ollerenshaw and Costello 2008). Worst, the projectile can be destabilized if a large force is applied near its nose (Lloyd and Brown 1979). This paper specifically studies four different concepts of CCCF in order to identify, under the proposed guidance and control algorithms, the best choice. To properly operate the fuzes, guidance, navigation, and control (GNC) algorithms are required.

Projectile guidance algorithms usually fit in one of the three following categories: trajectory shaping, trajectory tracking, or predictive guidance. Trajectory shaping algorithms (Park et al. 2011) compute a new nonballistic trajectory. This method generally requires a high level of maneuverability, which is difficult to achieve with canards control on a spin-stabilized projectile. Trajectory tracking (Rogers and Costello 2010; Robinson and Strömbäck 2013) consists in following the expected ballistic trajectory. This type of guidance is easy to implement, but tends to require higher control effort through the whole flight than predictive guidance (Teofilatto and De Pasquale 1998). Predictive guidance (Calise and El-Shirbiny 2001; Fresconi 2011) uses a ballistic model of the projectile to estimate its point of impact (PoI) and compute corrections accordingly. The precision of this method is, therefore, highly affected by the model (Fresconi et al. 2011). In order to include the drifting motion of the spin-stabilized projectile in the trajectory prediction, the modified point mass model (Lieske and Reiter 1966) is used in the proposed predictive guidance algorithm.

[1]Defence Scientist, Weapons Systems, Defence Research and Development Canada, 2459 de la Bravoure Rd., Quebec City, QC, Canada G3J 1X5 (corresponding author). E-mail: Eric.Gagnon@drdc-rddc.gc.ca

[2]Research Engineer, Numerica Technologies Inc., 3420 rue Lacoste, Quebec City, QC, Canada G2E 4P8. E-mail: Alexandre.Vachon.NUMERICA@drdc-rddc.gc.ca

Note. This manuscript was submitted on July 3, 2015; approved on March 9, 2016; published online on July 11, 2016. Discussion period open until December 11, 2016; separate discussions must be submitted for individual papers. This paper is part of the ***Journal of Aerospace Engineering***, © ASCE, ISSN 0893-1321.

The first works studying spin-stabilized projectile control algorithms are based on decoupled lateral and vertical axis controllers, similar to missiles autopilot design, and use simple linear control techniques: integrator on acceleration (Calise and El-Shirbiny 2001) or loop-shaping on pitch/yaw rates (Gagnon and Lauzon 2008). Recently, more-advanced control techniques, multivariate filtered proportional-integral-derivative controller (Theodoulis et al. 2013b) and H_∞ synthesis (Theodoulis et al. 2015) on load factors and pitch/yaw rates, and linear-quadratic synthesis (Fresconi et al. 2015) on accelerations and pitch/yaw rates, are applied on a model derived from the complete seven-degrees-of-freedom (DoF) dynamic of the projectile. However, as the main objective of this work is not the development of a control algorithm, a simple and versatile autopilot is designed by poles/zeros cancellation on, similar to early works, a linearized six-DoF model with decoupling of the lateral and vertical axes. Furthermore, as the concepts are not equipped with inertial measurement devices, the control function is designed to manage only the accelerations. For the CCCF concept requiring projectile drag control, a proportional integrator scheme is also developed.

The navigation function, which uses the sensor measurements to estimate the position, velocity, acceleration, and spin rate of the projectile, does not differ from navigation algorithm of other flying vehicles where various types of Kalman filter are used. Kalman filters are the subject of extensive research in the area of autonomous and assisted navigation (Welch and Bishop 2006), and are also used for guided projectile applications (Fairfax and Fresconi 2012). This work does not focus on the navigation aspects and, therefore, employs only a linear Kalman filter to perform the navigation task.

The objective of this paper being a relative comparison between the CCCF concepts, the proposed GNC algorithms were chosen for their versatility and simplicity. They are not necessarily to the level of the latest algorithms in their respective fields, but they are suitable for the comparison. The obtained results are therefore nuanced with respect to the algorithms. Those results are obtained by simulations of a pseudo-seven-degrees-of-freedom (7DoF) simulator of a spin-stabilized projectile equipped with the four studied CCCF concepts. A pseudo-7DoF simulator is a 7DoF model (Costello and Peterson 2000) in which one DoF, the fuze spin rate, is varied without any dynamics. Therefore, no control loop, as developed by Theodoulis et al. (2013a), is required for this channel.

Concepts Descriptions

The four concepts of course correction fuzes have a similar design. The fuzes are equipped with four identical canards mounted on a despun ring (Fig. 1).

All the canards have the same trapezium-shaped planar area and diamond airfoil (Fig. 2). The fuze dimensions and weight repartition are also identical for the four types of CCCF.

The ring is free to rotate, and its spin rate is controlled by modifying the counter-electromotive torque of an alternator. Since the alternator is a unidirectional actuator, an external torque is required to move the fins ring in the opposite direction. This external torque is generated by the canards differential deflection. Before the starting point of the guided flight, the spin rate is held constant. Therefore, over a complete cycle, the canards do not generate a residual lifting force. During the guided portion of the flight, the spin rate is forced at 0 and, as a pseudo-7DoF model is used, the fins ring is immediately positioned at the desired roll angle.

The fuzes are equipped with a global positioning system (GPS) receiver and an algorithm, which have the capability to determine

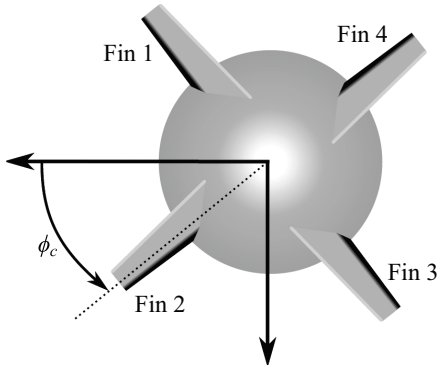

Fig. 1. Front view of canards-based course correction fuze, showing positive deflection angle

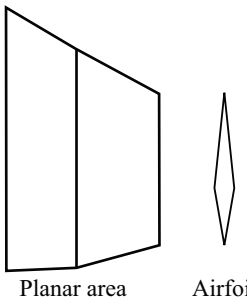

Fig. 2. Canards shape schematic

the spin rate and roll angle of the projectile. Combined with a rotary encoder, the spin rate and roll angle of the fins ring can be estimated. As the GPS receiver measures the projectile position and velocity only, a Kalman filter is required to estimate its acceleration. Furthermore, as no inertial measurements are available, the navigation function cannot estimate the projectile pitch, yaw, and their rates.

The fuzes are installed on a typical 155-mm spin-stabilized shell to form the guided projectile. The aerodynamic coefficients of the shell and of the fins ring are computed independently. The shell coefficients, obtained with *PRODAS version 3.5.3*, are stored in three-dimensional tables, decomposed in terms of the Mach number, total angle of attack, and aerodynamic roll angle. On their part, the fins ring coefficients form seven-dimensional tables obtained from the subtraction of two sets of Missile Datcom (Rosema et al. 2011) predictions, one set representing the projectile equipped with a CCCF and the other representing the projectile equipped with a conventional fuze. Therefore, the aerodynamic interactions between the fins ring and the projectile body are encapsulated in the fins ring coefficients. The fins ring tables are function of the Mach number, total angle of attack, aerodynamic roll angle, and four canards deflection angle. At very high deflection angles, required for Concept 4, the aerodynamics exhibit a nonlinear behavior. As the simulator estimates the coefficients with linear interpolation between the flight condition points, the gap between consecutive deflection angles has been tightened in order to capture, as much as possible, this nonlinear behavior.

Changeable Roll Angle Ring Equipped with Four Fixed Canards (Concept 1)

This concept is composed of four canards fixed at the same deflection angle. In order to produce a torque around the projectile spin

axis which despins the fins ring, two opposite canards, Fins 2 and 4, are deflected positively (Fig. 1). The two other canards are deflected in opposite directions: Fin 1 is positively deflected while Fin 3 deflection is negative. They produce a lifting aerodynamic control force that is oriented by changing the fins ring roll angle, controlled by the counter-electromotive torque of an alternator.

Changeable Roll Angle Ring Equipped with Two Fixed Canards and Two Actuated Canards (Concept 2)

The only difference between this concept and the previous one is in the maneuvering canards, Fins 1 and 3. In this concept, their deflection angle is modulated by an actuator. In order to be coherent in the comparison, their maximal deflection angle is identical to the deflection angle of Concept 1. Fins 2 and 4 remain fixed and the roll angle of the fins ring is still controlled by the counter-electromotive torque of an alternator.

Regulated Roll Angle Ring Equipped with Four Actuated Canards Having Similar Deflection Limits (Concept 3)

This concept is based on complete decoupling of vertical and lateral maneuvers. One pair of actuated canards, Fins 1 and 3, generates the lateral maneuvers, while the other pair generates the vertical ones. The canards of each pair are deflected in opposite directions to produce an aerodynamic control force perpendicular to the projectile spin axis. In order to be coherent in the comparison, the maximal deflection angle is similar to the deflection angle of Concept 1. The despun torque is obtained by a bias of 0.5°, in positive direction, on the deflection angle of each canard. The counter-electromotive torque of an alternator is used to maintain the fins ring roll angle at 0° once the fuze is activated.

Regulated Roll Angle Ring Equipped with Four Actuated Canards Having Different Deflection Limits (Concept 4)

This concept modulates the projectile drag by deflecting one pair of canards, Fins 2 and 4, to high deflection angles. By controlling the drag, these canards provide maneuverability along the longitudinal axis. Their maximal deflection angle is set at 44.5°, generating a range similar to those of the other concepts. The lateral maneuvers are obtained by the other pair of canards, Fins 1 and 3, which are deflected in opposite directions in order to generate an aerodynamic control force perpendicular to the projectile spin axis. In order to be consistent, their maximal deflection angle is identical to the deflection angle of Concept 1. As for Concept 3, the despun torque is obtained by a bias of 0.5°, in a positive direction, on the deflection angle of each canard. Once the fuze is activated, the fins ring is maintained at 0° of roll angle by controlling the counter-electromotive torque of an alternator.

Summary of Concepts Characteristics

Table 1 presents the canards deflection ranges and required actuators, canards deflection actuator (CDA), and counter-electromotive actuator (CEA), for each concept. For the actuated concepts, the canards of a pair (Fins 1 and 3 or Fins 2 and 4) are connected on the same actuator and therefore move simultaneously. This work does not study how the required actuators can be included in the fuze, but assumes that it is feasible.

Table 1. Actuators and Canards Deflection Ranges for Each Concept

Concept	Actuators	Canards deflection ranges			
		Fin 1 [°]	Fin 2 [°]	Fin 3 [°]	Fin 4 [°]
1	1 CEA	8	8	−8	8
2	1 CEA, 1 CDA	[−8, 8]	8	[−8, 8]	8
3	1 CEA, 2 CDAs	[−7.5, 8.5]	[−7.5, 8.5]	[−7.5, 8.5]	[−7.5, 8.5]
4	1 CEA, 2 CDAs	[−8, 8]	[0.5, 44.5]	[−8, 8]	[0.5, 44.5]

Autopilot Design

Concepts 1–3 use the same autopilot duplicated on two control axes. The first one manages the acceleration along the vertical axis, while the second autopilot works along the lateral axis. This autopilot is developed in order to manage the acceleration with a pair of canards generating a force perpendicular to the projectile spin axis. On its part, as it is equipped with a pair of canards configured in order to generate a force parallel to the projectiles spin axis, the vertical autopilot of Concept 4 is replaced by an autopilot managing the axial acceleration.

Lateral and Vertical Axes Autopilots

The first step in developing an autopilot is to obtain a mathematical representation of the projectile. As the autopilot has to work with the projectile rotational and translation motions, a complete 6DoF nonspinning model (Wernert et al. 2010) is required. The proposed model includes the normal force (C_{N_α}), Magnus force ($C_{N_{pa}}$), pitching/yawing moment (C_{m_α}), Magnus moment ($C_{m_{pa}}$), and pitch/yaw damping moment (C_{mq}). Assuming a symmetrical projectile with small angle of attack and sideslip angle, the state space representation of the equations of motion is (Calise and El-Shirbiny 2001)

$$\begin{bmatrix} \dot{\alpha} \\ \dot{\beta} \\ \dot{q} \\ \dot{r} \end{bmatrix} = \begin{bmatrix} Z_\alpha & Z_m & 1 & 0 \\ -Z_m & Z_\alpha & 0 & -1 \\ M_\alpha & M_m & M_q & -\dfrac{pI_x}{I_y} \\ M_m & -M_\alpha & \dfrac{pI_x}{I_y} & M_q \end{bmatrix} \begin{bmatrix} \alpha \\ \beta \\ q \\ r \end{bmatrix} + \begin{bmatrix} 0 & Z_c \\ Z_c & 0 \\ 0 & M_c \\ -M_c & 0 \end{bmatrix} \begin{bmatrix} f_y \\ f_z \end{bmatrix} \tag{1}$$

where

$$Z_\alpha = -\frac{\bar{q} s_r C_{N_\alpha}}{m|\mathbf{v}|} \tag{2}$$

$$Z_m = \frac{\bar{q} s_r d_r p C_{N_{pa}}}{m|\mathbf{v}|^2} \tag{3}$$

$$M_\alpha = \frac{\bar{q} s_r d_r C_{m_\alpha}}{I_y} \tag{4}$$

$$M_m = \frac{\bar{q} s_r d_r^2 p C_{m_{pa}}}{I_y|\mathbf{v}|} \tag{5}$$

$$M_q = \frac{\bar{q} s_r d_r^2 C_{mq}}{I_y|\mathbf{v}|} \tag{6}$$

$$Z_c = \frac{1}{m|\mathbf{v}|} \tag{7}$$

$$M_c = \frac{l_f}{I_y} \tag{8}$$

and s_r and d_r are the referential area and referential diameter of the projectile, respectively; m its mass; $\mathbf{v}$ its velocity vector; p its spin rate; I_x its inertia around its spin axis; I_y its inertia around its pitch/yaw axis; $\bar{q}$ is the dynamic pressure; l_f is the distance, along the projectile spin axis, between the fins center of pressure and projectile center of gravity; and inputs f_y and f_z are the magnitudes of the lateral and vertical aerodynamic control forces.

The controlled variables being the lateral and vertical accelerations, the output equation of the state space representation is

$$\begin{bmatrix} a_y \\ a_z \end{bmatrix} = \begin{bmatrix} -Z_m|\mathbf{v}| & Z_\alpha|\mathbf{v}| & 0 & 0 \\ Z_\alpha|\mathbf{v}| & Z_m|\mathbf{v}| & 0 & 0 \end{bmatrix} \begin{bmatrix} \alpha \\ \beta \\ q \\ r \end{bmatrix} + \begin{bmatrix} Z_c|\mathbf{v}| & 0 \\ 0 & Z_c|\mathbf{v}| \end{bmatrix} \begin{bmatrix} f_y \\ f_z \end{bmatrix} \tag{9}$$

An analysis of the Relative Gain Array supports the pairing of the vertical force with the vertical acceleration, and the lateral force with the lateral acceleration. The cross axis relative gains being smaller than 0.33 for all the domain of operation, a decentralized controller using direct axis is then designed. A multivariable controller, as in Theodoulis et al. (2015), or the implementation of decouplers (Gagnon et al. 1998) might improve the autopilot performance, but they are not mandatory. Furthermore, the transfer functions of the dominant pairings are identical; an autopilot can then be designed for one axis and duplicated on the other.

The aerodynamic coefficients and, hence the Z and M variables, vary as a function of the projectile airspeed, spin rate, and altitude. Therefore, the autopilots must be scheduled to match the model variations generated by these three parameters.

The vertical axis transfer function, extracted from the state space representation, can be represented by the following transfer function:

$$G_{p_z}(s) = \frac{a_z}{f_z} = \frac{(s^2 + 2\zeta_3\omega_3 s + \omega_3^2)(\frac{s}{\omega_4} + 1)(-\frac{s}{\omega_5} + 1)}{(s^2 + 2\zeta_1\omega_1 s + \omega_1^2)(s^2 + 2\zeta_2\omega_2 s + \omega_2^2)} \tag{10}$$

Here, the location of the poles and zeros is interesting. The complex zeros, defined by their natural frequency, ω_3, damping factor, ζ_3, and a pair of complex poles (ω_1 and ζ_1) have a high natural frequency and are located near each other. The other complex poles have a much smaller natural frequency (ω_2).

The proposed autopilot is obtained by poles/zeros cancellation enhanced by an integrator to ensure no static error. As the high-frequency poles and zeros are much higher in frequency than the achievable closed-loop dynamics and are close enough to naturally cancel each other, they are omitted in the cancellation process. The unstable zero cannot be canceled, but a stable pole is added at the same frequency to reduce high-frequency noise. The resulting autopilot is therefore

$$G_{c_z}(s) = \frac{f_z}{a_{c_z} - a_z} = \frac{k_c(s^2 + 2\zeta_2\omega_2 s + \omega_2^2)}{\left(\frac{s}{\omega_4} + 1\right)\left(\frac{s}{\omega_5} + 1\right)s} \tag{11}$$

The autopilot gain (k_c) is chosen to obtain a phase margin of 60°. Gain margin is not enforced during autopilot design, but an analysis of the controller shows that, for all the design points, the margin is always greater than 6 dB. The combination of both margins ensures some robustness properties.

The projectile being considered symmetrical, and the lateral axis autopilot is identical

$$G_{c_y}(s) = \frac{f_y}{a_{c_y} - a_y} = \frac{k_c(s^2 + 2\zeta_2\omega_2 s + \omega_2^2)}{\left(\frac{s}{\omega_4} + 1\right)\left(\frac{s}{\omega_5} + 1\right)s} \tag{12}$$

The autopilots are scheduled to match the variations of the Z and M variables due to the projectile airspeed, spin rate, and altitude evolution. Those variations are visible in the transfer function gain, and in the natural frequency and damping factor of the poles and zeros. Autopilot sequencing is done by linear interpolation of those variables (k_c, ω_2, ω_4, ω_5, and ζ_2) between the selected design points. Ten points, evenly spaced between the minimal and maximal values of the conventional projectile flight envelope, are selected for each of the three sequencing parameters. With this approach, all the parameters combinations must be computed, even if some are not expected to happen.

The robustness properties of the controllers are validated by a μ-analysis, for robust performance, on the multivariable system. Uncertainties of 40% on the Magnus, 10% on the pitch/yaw damping and control forces, and 5% on the other aerodynamic coefficients (Theodoulis et al. 2015) are considered in the analysis, and the desired performances are those of the nominal closed-loop responses for all flight conditions. The μ-analysis is conducted at different flight times of the guided portion of the high quadrant elevation (QE) referential trajectory. The resulting contour plot of the structured singular value upper bound for robust performance is presented in Fig. 3. As the bound is below the unity for all flight times and frequencies, robust performance over the entire trajectory is ensured.

Concept 1 Control Function Output

For this concept, only the fins ring roll angle is controlled. To be coherent with the orientation defined in Fig. 1, the fins ring roll angle is obtained by mixing the lateral and vertical autopilots output

$$\phi_c = \pi + \arctan\frac{f_z}{f_y} \tag{13}$$

Concept 2 Control Function Outputs

The fins ring roll angle of this concept is also generated with Eq. (13), and the magnitude of the aerodynamic control force is

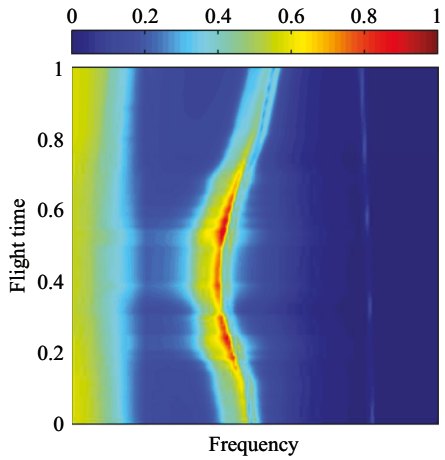

Fig. 3. (Color) μ-plot of robust performance along the high QE referential trajectory

modulated by the deflection angle of the maneuvering canards. The lift generated by one fin can be approximated by

$$f_l = \bar{q} s_{r_f} C_{N_\delta} \delta \tag{14}$$

Based on this approximation, the deflection angle of the maneuvering fins (Fins 1 and 3) is computed as

$$-\delta_1 = \delta_3 = \frac{\sqrt{f_y^2 + f_z^2}}{\bar{q}(2 s_{r_f}) C_{N_\delta}} \tag{15}$$

where s_{r_f} is the aerodynamic referential area of a fin. The sign inversion between Fins 1 and 3 comes from the sign convention of Fig. 1.

Concept 3 Control Function Outputs

In this concept, the autopilots output are not mixed. They are rather directly used to determine the required deflection angles for both pairs of canards. Considering the approximation of Eq. (14) for the lift force, the deflection angle of the lateral axis fins (Fins 1 and 3) and of the vertical axis fins (Fins 2 and 4) are computed as

$$\delta_1 = -\frac{f_y}{\bar{q}(2 s_{r_f}) C_{N_\delta}} + 0.5 \qquad \delta_3 = \frac{f_y}{\bar{q}(2 s_{r_f}) C_{N_\delta}} + 0.5 \tag{16}$$

$$\delta_2 = -\frac{f_z}{\bar{q}(2 s_{r_f}) C_{N_\delta}} + 0.5 \qquad \delta_4 = \frac{f_z}{\bar{q}(2 s_{r_f}) C_{N_\delta}} + 0.5 \tag{17}$$

The sign inversions between Fins 1 and 3 and between Fins 2 and 4 come from the sign convention of Fig. 1, while the offset of 0.5° on each canard is applied to despin the fins ring.

Longitudinal Autopilot

As the projectile rotational motion has only a small influence on its axial airspeed, Newton's second law can be used to describe the longitudinal transfer function, which is therefore a single gain corresponding to the inverse of the projectile mass

$$G_{p_x}(s) = \frac{a_x}{f_x} = \frac{1}{m} \tag{18}$$

As a result, a nonscheduled, unitary gain, proportional integrator autopilot is sufficient to control the projectile axial motion

$$G_{c_x}(s) = \frac{f_x}{a_{c_x} - a_x} = \frac{\tau s + 1}{\tau s} \tag{19}$$

The integrator time constant, τ, is set in order to obtain a settling time of approximately 1 s.

Concept 4 Control Function Outputs

For the lateral axis, the autopilot of Eq. (12) is implemented, and Eq. (16), without the 0.5° offset, is used to compute the canards deflection angle from the autopilot output.

Assuming that the drag force of a fin can be computed by

$$f_d = \bar{q} s_{r_f} (C_{D_\delta} \delta^2 + C_{D_0}) \tag{20}$$

Then, the deflection angle of Fins 2 and 4 is

$$\delta_d = \delta_2 = \delta_4 = \sqrt{\frac{f_x - \bar{q}(2 s_{r_f}) C_{D_0}}{\bar{q}(2 s_{r_f}) C_{D_\delta}}} \tag{21}$$

Guidance Algorithm

The guidance algorithm is responsible for determining the actions required to reach the target. The proposed algorithm is based on the computation of zero-effort misses (ZEMs) from predicted impact locations. These ZEMs are converted into acceleration setpoints for the autopilots.

The guidance algorithm is based only on the translational motion of the projectile, which can be modeled by a point mass affected by external forces. These forces are the gravity, drag, lift, and Magnus.

The drag force acts in the opposite direction of the projectile velocity

$$\boldsymbol{f_D} = -\frac{\bar{q} s_r C_D}{m} \frac{\mathbf{v}}{|\mathbf{v}|} \tag{22}$$

The lift force is parallel to the yaw of repose vector ($\boldsymbol{\alpha_r}$)

$$\boldsymbol{f_L} = \frac{\bar{q} s_r C_{L_\alpha}}{m} \boldsymbol{\alpha_r} \tag{23}$$

where the latter can be modeled as (McCoy 2012)

$$\boldsymbol{\alpha_r} = \frac{I_x p}{\bar{q} s_r d_r C_{m_\alpha}} \left(\mathbf{g} \times \frac{\mathbf{v}}{|\mathbf{v}|} \right) \tag{24}$$

The Magnus force is perpendicular to the plane formed by the velocity and yaw of repose vectors

$$\boldsymbol{f_M} = \frac{\bar{q} s_r C_{N_{pa}}}{m} \frac{p d_r}{|\mathbf{v}|} \left(\frac{\mathbf{v}}{|\mathbf{v}|} \times \boldsymbol{\alpha_r} \right) \tag{25}$$

In the previous equations, C_D, C_{L_α}, $C_{N_{pa}}$, and C_{m_α} are the aerodynamic coefficients, namely drag coefficient, lift coefficient due to the angle of attack, Magnus force coefficient, and pitching moment coefficient due to the angle of attack. The gravity vector ($\mathbf{g}$) is assumed to be constant at 9.81 m/s^2 and is always pointing downwards.

In order to consider the drifting motion inherent to a spin-stabilized projectile, the modified point mass equation (Lieske and Reiter 1966) is used in a line-of-sight (LoS) coordinate system. This system has its x-axis and y-axis in the horizontal plane. Its x-axis is parallel to the cannon muzzle azimuth and points downrange, while its y-axis points to the right when looking downrange. Its z-axis completes the right-handed system and points downwards. The system origin is the launch point. The modified point mass equation is

$$m\dot{\boldsymbol{v}} = \boldsymbol{f_D} + m\mathbf{g} + \boldsymbol{f_L} + \boldsymbol{f_M} \tag{26}$$

Impact Location Prediction

The guidance algorithm begins by estimating the time to go, i.e., the time required to reach the target altitude. To obtain it, the vertical velocity differential equation, the third component of Eq. (26), is used. Along the LoS frame's z-axis, the lift and Magnus forces are much smaller than the drag and gravity forces. Therefore, they can be neglected and the velocity derivative becomes

$$\dot{v}_z = -\frac{\bar{q} s_r C_D}{m|\mathbf{v}|} v_z + g \tag{27}$$

Considering the drag coefficient and projectile airspeed constant for the rest of the flight, $\bar{q} s_r C_D / m|v|$ becomes a constant denoted by d in the following. Eq. (27) is then a time linear equation and can be integrated from the current time ($t = 0$) until the time to go ($t = t_{go}$)

$$v_z(t_{go}) - v_z(0) = -d(z_T - z(0)) + gt_{go} \tag{28}$$

where z_T is the target altitude, which is considered null in the following. By considering Eq. (27) as a time-invariant linear differential equation, it can be solved by an exponential. Specifically, at $t = t_{go}$, it becomes

$$v_z(t_{go}) = v_z(0)e^{-dt_{go}} + \frac{g(1 - e^{-dt_{go}})}{d} \tag{29}$$

Eq. (28) is introduced in Eq. (29), and the resulting equation is reorganized to form a transcendental equation in t_{go}

$$t_{go} = \frac{\ln\left(\frac{dz(0)+gt_{go}+v_z(0)-\frac{g}{d}}{v_z(0)-\frac{g}{d}}\right)}{-d} \tag{30}$$

This equation can be solved iteratively using a Newton-Raphson scheme. With a good initial guess, it takes fewer than five iterations to solve it at a precision of 0.01 s. At the first call of the guidance law, the expected time to go of the referential trajectory can be used for this initial guess. In the following calls, the time to go of the previous solution is used as actual initial guess.

This estimated time to go is used to compute the impact location in the horizontal plane. The projectile motion along the LoS frame x-axis is not significantly affected by the Magnus, gravity, and lift forces. As a result, the first component of Eq. (26) can be written as

$$\dot{v}_x = -dv_x \tag{31}$$

Considering Eq. (31) as a time-invariant linear differential equation, its solution at $t = t_{go}$ is an exponential

$$v_x(t_{go}) = v_x(0)e^{-dt_{go}} \tag{32}$$

Eq. (31) can also be integrated from the current time ($t = 0$) up to the time to go ($t = t_{go}$)

$$v_x(t_{go}) - v_x(0) = -d(x(t_{go}) - x(0)) \tag{33}$$

Combining Eqs. (32) and (33), the estimated longitudinal impact position is

$$x(t_{go}) = x(0) - \frac{v_x(0)e^{-dt_{go}} - v_x(0)}{d} \tag{34}$$

For the motion along the lateral axis, the Magnus and lift forces must be considered. The second component of Eq. (26) is then

$$\dot{v}_y = -dv_y + \frac{C_{L_\alpha} I_x pg}{C_{m_\alpha} d_r m|\mathbf{v}|^2} v_x - \frac{C_{N_{pa}} p^2 I_x g}{C_{m_\alpha} m|\mathbf{v}|^4} v_y v_z \tag{35}$$

The velocity along the y-axis is coupled with those of the x-axis and z-axis. With this coupling, an analytic solution of Eq. (35) is difficult to establish. However, the estimated lateral position at impact can be approximated by a time second-order polynomial

$$y(t) = \dot{v}_y(0)t^2 + v_y(0)t + y(0) \tag{36}$$

where $\dot{v}_y$ is obtained from Eq. (35). Then, the estimated lateral position at impact becomes

$$y(t_{go}) = \left(-dv_y(0) + \frac{C_{L_\alpha} I_x pg}{C_{m_\alpha} d_r m|\mathbf{v}|^2} v_x(0) - \frac{C_{N_{pa}} p^2 I_x g}{C_{m_\alpha} m|\mathbf{v}|^4} v_y(0)v_z(0)\right) t_{go}^2 + v_y(0)t_{go} + y(0) \tag{37}$$

From the current projectile state, defined by its position [$\boldsymbol{x}(0)$] and velocity [$\boldsymbol{v}(0)$] vectors, the impact location is then obtained by estimating the time to go with Eq. (30), which is introduced in Eqs. (34) and (37) to obtain the estimated longitudinal and lateral positions at impact.

Dual Regime Algorithm

The PoI predictions are based on the hypothesis that the aerodynamic coefficients are constant for the whole flight, which is obviously not the case. Projectile aerodynamics vary significantly with the Mach number and exhibit two distinct behaviors, depending on whether the projectile is subsonic or supersonic. Also, once the projectile gets to a subsonic regime, it should not return to supersonic speed later in its flight. Therefore, to improve the predictions, two sets of constant aerodynamic coefficients are used. The projectile state at the end of the supersonic flight is predicted with one set and, from there, the PoI is predicted with the other set. From the referential trajectory, the time at which the projectile becomes subsonic (t_{m1}) can be estimated and used to compute the supersonic time to go

$$t_s = t_{m1} - t_0 \tag{38}$$

The supersonic time to go is used in Eqs. (29), (32), (34), and (37) to obtain, respectively, the vertical velocity, axial velocity, axial position, and lateral position of the projectile when it falls below the sonic barrier. To be coherent with the time second-order polynomial approximation of the crossrange position, the crossrange velocity is approximated by a time first-order polynomial

$$v_y(t_{m1}) = \left(-dv_y(0) + \frac{C_{L_\alpha} I_x pg}{C_{m_\alpha} d_r m|\mathbf{v}|^2} v_x(0) - \frac{C_{N_{pa}} p^2 I_x g}{C_{m_\alpha} m|\mathbf{v}|^4} v_y(0)v_z(0)\right) t_s + v_y(t_0) \tag{39}$$

On its part, the vertical position is obtained by combining Eqs. (28) and (29)

$$z(t_{m1}) = z(0) - \frac{v_z(0)(e^{-dt_s} - 1) + g(\frac{1-e^{-dt_s}}{d} - t_s)}{d} \tag{40}$$

The six components of the position and velocity vectors at the end of the supersonic regime are then known and used as initial state of the algorithm to perform the impact location prediction. When the projectile is subsonic at the initial time, the prediction algorithm is used directly on the measured projectile position and velocity, eliminating the supersonic prediction step.

Zero-Effort Misses Estimation

The zero-effort misses are obtained by subtracting the target longitudinal (x_T) and lateral (y_T) positions from the predicted longitudinal and lateral positions of the PoI

$$\mathrm{ZEM}_y = y(t_{go}) - y_T \tag{41}$$

$$\mathrm{ZEM}_x = x(t_{go}) - x_T \tag{42}$$

The impact location predictions based on the modified point mass model significantly differ from those based on the complete 6DoF model (Fresconi et al. 2011). To mitigate this issue, the target position is predicted at the same rate and with the same prediction model as the PoI, but with its current state obtained from the referential trajectory.

The resulting ZEMs are converted into autopilot acceleration setpoints. For Concept 4, the conversion is

$$\boldsymbol{a}_{\boldsymbol{go}} = k_g[-\mathrm{ZEM}_x \quad -\mathrm{ZEM}_y \quad 0]^T \tag{43}$$

This conversion gives a setpoint for the longitudinal autopilot, and another for the lateral one.

The three other concepts require a setpoint along the vertical axis rather than along the longitudinal one. As a force along the vertical axis modifies the longitudinal impact location, the longitudinal ZEM is converted in a vertical acceleration setpoint. In the ascending phase of high QE launch, a negative force in the vertical axis decreases the projectile impact location, the acceleration setpoint must then be inversed. For high QE descending portion and for low QE launch, a negative force in the vertical axis increases the projectile longitudinal impact location, a sign inversion is therefore not required in the setpoint

$$\boldsymbol{a}_{\boldsymbol{go}} = \begin{cases} k_g[0 \quad -\mathrm{ZEM}_y \quad -\mathrm{ZEM}_x]^T & \text{if } \gamma_l > 45° \text{ and } \gamma > 0 \\ k_g[0 \quad -\mathrm{ZEM}_y \quad \mathrm{ZEM}_x]^T & \text{otherwise} \end{cases} \tag{44}$$

where γ_l is the launch QE, in degrees, and γ is the flight path angle.

The guidance gain, k_g, which appears in both conversions, is the tuning parameter of the guidance algorithm. An optimization routine based on the bisection method has been created in order to find the value of the gain that minimizes the circular error probability (CEP), evaluated from Monte-Carlo runs of 100 simulations. A different optimization is run for each concept and for each firing condition.

Eqs. (43) and (44) represent the accelerations required to eliminate the ZEMs. However, there is also expected acceleration coming from the projectile aerodynamics and gravity. These two acceleration components are estimated with the same variables as the impact location estimation

$$a_{eo} = \frac{\bar{q} s_r \left(-C_D \frac{v_o}{|\mathbf{v}|} + C_{L_\alpha} \alpha_{ro} + \frac{d_r p C_{N_{pa}}}{|\mathbf{v}|} \left(\frac{v_o}{|\mathbf{v}|} \times \alpha_{ro} \right) \right)}{m} + g_o \tag{45}$$

The expected acceleration is added to the acceleration setpoints [Eqs. (43) or (44)] in order to reduce autopilot workload.

Results

The previous algorithms are implemented into a pseudo-7DoF simulator of a typical 155-mm shell equipped with a CCCF, which can be configured to represent any of the four proposed concepts. The simulator is implemented in a nonspinning reference frame (Wernert et al. 2010), with constant gravity and U.S. Standard 1976 atmospheric model.

Different factors may contribute to projectile dispersion. The factors simulated are the winds, muzzle velocity, and gun aiming. Table 2 offers the standard deviation applied on each of them. The winds are constant and their magnitudes are relative to the most recent meteorological measurements, which are compensated by the muzzle alignment.

Table 2. Standard Deviations of Considered Perturbations

Perturbation	Standard deviation
Crossrange wind velocity	3 m/s
Downrange wind velocity	3 m/s
Muzzle velocity	2 m/s
Firing azimuth	1 mils
Quadrant elevation angle	1.5 mils

The first series of tests studies the footprints of the CCCF concepts to see which one better matches the conventional projectile dispersion. The second series of tests studies guided projectiles dispersion and range, through Monte-Carlo simulations realized with the perturbation standard deviations given in Table 2. Each series of tests is done at two different quadrant elevations, one under 800 mils, considered as the low QE case, and the other one over 800 mils, considered the high QE case. Prior to these two series of tests, an analysis of the time history of the projectile and algorithms parameters for typical guided flights was conducted. This analysis did not show any problematic behavior or tendencies to bring the projectile close to instability.

The fuze activation time is dictated by the GPS receiver lock time and the flight-path inclination. The GPS receiver must be locked and the projectile must have reached a given flight-path angle before starting the guided flight. This flight-path angle is chosen in order to maximize fuze efficiency. During the unguided flight and for the referential trajectory generation, the canards are fixed in order to minimize the drag. Therefore, the PoI of the referential trajectory, which represents the target location, differs for each concept.

Footprint Analysis

The footprint of a projectile equipped with a CCF corresponds to the displacement achievable with this type of fuze. It is obtained by fixing the control variables at their extrema for the whole duration of the guided flight. If a projectile equipped with a conventional fuze lands inside the guided projectile footprint, the CCF should have enough control authority to compensate for the disturbances and directly hit the target. However, because of sensor imperfections, guidance and control limitations, and the lack of ability to fully compensate for perturbations occurring late in the flight, a perfect hit rarely occurs. In theory, the optimal CCF design is obtained when its footprint area perfectly fits the conventional fuze dispersion pattern.

The footprint is composed of the results of unperturbed simulations. One simulation per control variable combination is run, and the points of impact (PoIs) of all combinations create the footprint. For Concepts 1 and 2, the footprint is driven only by the fins ring roll angle, which is incremented by a step of 2° between each simulation. For Concepts 3 and 4, the footprint is affected by the canards deflection angle. One set of canards is deflected to its maximal/minimal values, and the deflection angle of the other set is incremented by step of 0.5° between each simulation. The same process is then repeated with the second set of canards being kept at its extrema, while the first set is incremented by step of 0.5°. Figs. 4 and 5 present the obtained footprints for the four types of CCCF. They also include 1,000 PoIs obtained with a conventional fuze (yellow dots).

The graphics indicate a better potential for Concept 4 than for the three others. Its elongated footprint shape better fits the downrange dispersion of the conventional fuze. Based on the footprint analysis only, Concept 3 does not seem to provide a significant improvement over Concepts 1 or 2. Only a small area when both pairs of canards are close to their extrema is covered by Concept 3 and not by the two others. Obviously, actuating the canards does not change the footprint area; with the latter representing the maximal achievable displacement, the footprints of Concepts 1 and 2 are then strictly identical.

Monte-Carlo Simulations Results

The second series of tests simulates 4,000 perturbed guided rounds, 1,000 per fuze, for each firing condition. The conventional fuze simulations of the footprints analysis are also used in this section.

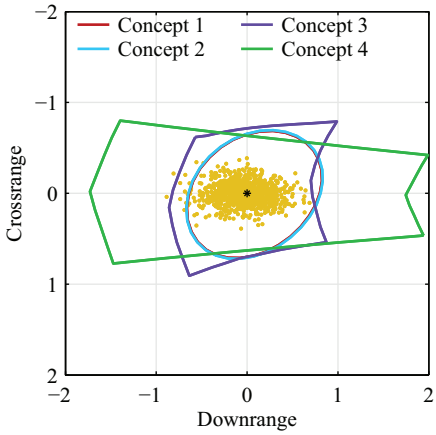

Fig. 4. (Color) CCCFs footprint and conventional PoIs at low QE

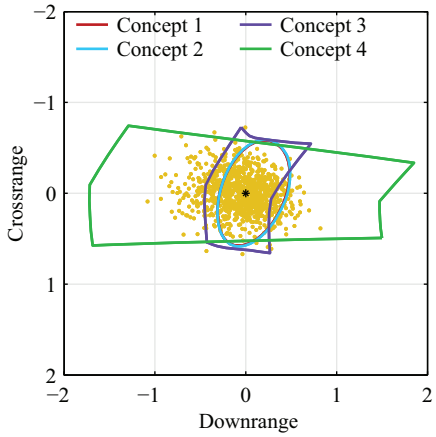

Fig. 5. (Color) CCCFs footprint and conventional PoIs at high QE

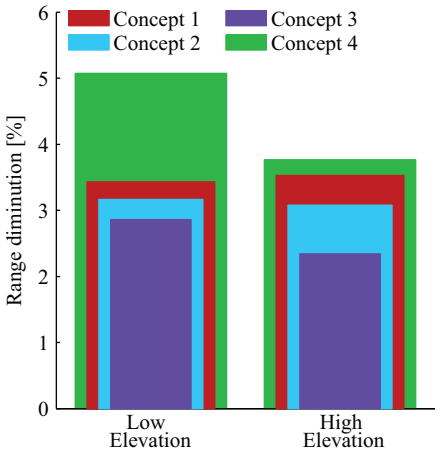

Fig. 6. (Color) Relative range diminution of the CCCFs

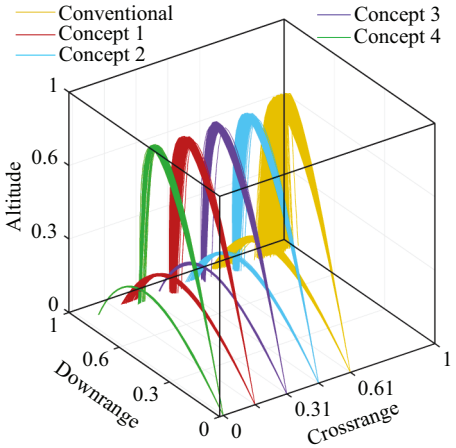

Fig. 7. (Color) Trajectories of the CCCFs and conventional fuze for both QEs

From these simulations, the range and precision of the fuzes are analyzed. Fig. 6 presents the range diminution of each CCCF, relative to the conventional fuze range, for both QEs.

The range being inversely proportional to the control surfaces deflection angles, Concept 4 should reach a shorter range than the other concepts. However, because all of its canards are set at smaller deflection angles during the unguided portion of the flight, the difference is not very significant. Similarly, due to the canards deflection angles during the unguided portion of the flight, Concept 3 reaches the longest range of the four proposed concepts, while Concept 2's range is slightly longer than that of Concept 1.

The resulting trajectories of both QEs are presented in Fig. 7. In this figure, the firing locations are located at 0 of downrange and distributed on the crossrange axis; each type of fuze is fired from a different crossrange.

For both QEs, the CCCFs trajectories are less dispersed than the conventional fuze ones, which is an indicator of the guidance and control algorithms efficiency. However, Fig. 7 does not give meaningful information about the precision at target. The analysis of the precision is initially done with the miss distance cumulative distribution. As guided projectiles are expected to have a concentration of misses close to the target, the usual CEP hides useful information required to draw conclusions about their performances. The miss distance cumulative distribution is a graphical representation of the percentage of rounds included in a circle. The graphic abscissa is the radius of the circle and its ordinate is the ratio of rounds that have landed in the corresponding circle's radius over the total number of rounds. The CEP is then the abscissa value for the 0.5 ratio. The graphics at low and high QE are, respectively, presented in Figs. 8 and 9. As expected, the four CCCF concepts are able to drastically increase the precision of a spin-stabilized projectile, but Concept 4 provides the highest precision level. For nearly all miss distances, its cumulative distribution is higher than the three other CCCF concepts. Concept 4's best precision is in line with that in Gagnon and Lauzon (2008), who states that continuous feedback control concept combining drag brake and spin brake, like Concept 4, is more precise than roll-decoupled CCF.

At low QE, Concept 3 is nearly as good as Concept 4, with the differences generated by the conventional PoIs very large misses, i.e., those impacting outside the Concept 3 footprint. Also, the performance gap between Concept 3 and Concepts 1 and 2 is larger than the footprints (Fig. 4) suggest. This is due to the guidance algorithm, which, because of the conventional PoIs dispersion, has the tendency to favor the longitudinal axis over the lateral one. At this elevation, the downrange ZEMs are larger than the lateral ones. As the guidance gain is the same for both axes [Eq. (44)], the guidance algorithm asks for larger corrections along the downrange axis. As the fins ring angle in Concepts 1 and 2 are based on the ratio of the two axes, the guidance algorithm then produces smaller corrections in the crossrange direction (Fig. 10). Furthermore, as

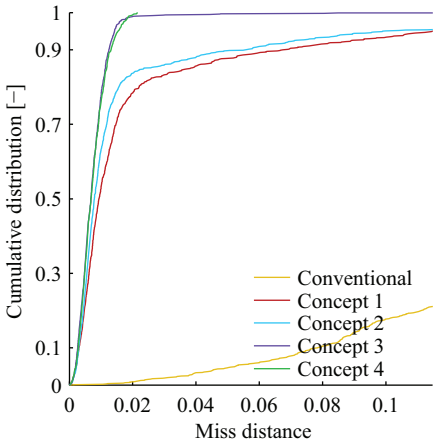

Fig. 8. (Color) Cumulative distribution of the CCCFs and conventional fuze at low QE

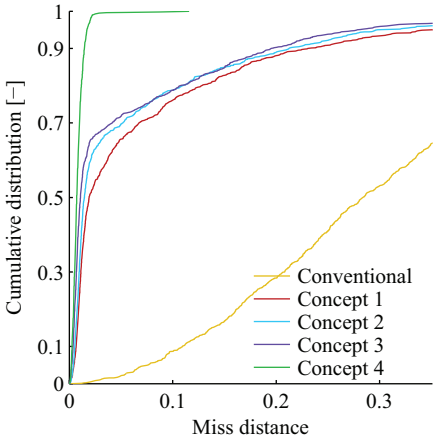

Fig. 9. (Color) Cumulative distribution of the CCCFs and conventional fuze at high QE

Concept 1's control force is not modulated, this concept tends to oscillate around the referential trajectory and to overcorrect the close misses, resulting in slightly lower precision than Concept 2.

At high QE, Concept 4 remains the best CCCF concept, and the performance gap with the other concepts is much more significant, which is coherent with the footprint patterns. Also, at this QE, the downrange ZEMs are marginally larger than the crossrange ones. The prioritization effect of the guidance law is, therefore, less significant. The axes decoupling of Concept 3 does not provide a significant improvement of the precision, in comparison to Concepts 1 and 2. As for the low QE tests, because of the inability to modulate its control force, Concept 1 has slightly larger misses than the other CCCF concepts.

A second way to analyze the precision of the CCCF concepts is by comparing the PoI patterns on a map centered on the target. Figs. 10 and 11 present those maps for both QE, revealing patterns that are coherent with the footprints and guidance law behavior.

At low QE, the PoIs of Concepts 3 and 4 are concentrated near the target. Concept 3 has a few residual misses corresponding to the conventional fuze misses impacting close or outside its footprint boundary. For their part, Concepts 1 and 2 have miss patterns that are largely due to the guidance algorithm which, as explained earlier, favors downrange corrections at this QE.

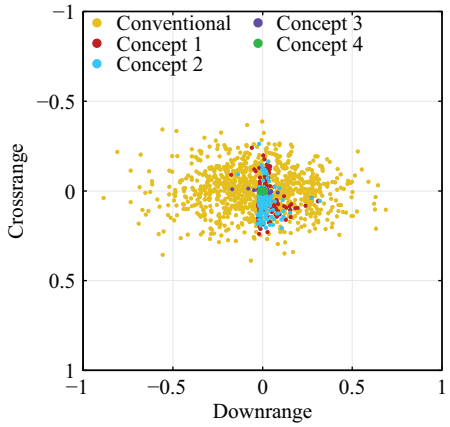

Fig. 10. (Color) PoIs of the CCCFs and conventional fuze at low QE

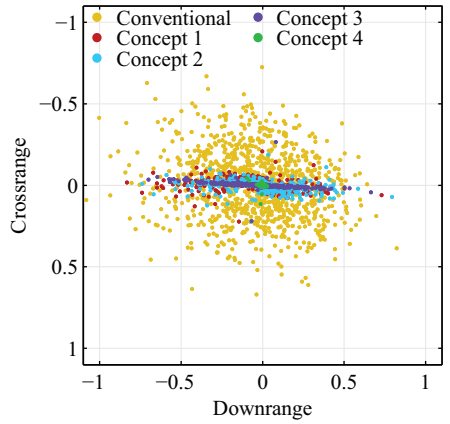

Fig. 11. (Color) PoIs of the CCCFs and conventional fuze at high QE

At high QE, Concept 4 has some residual misses in crossrange, which are related to the conventional fuze PoIs that are not covered by its footprint. For their part, Concepts 1, 2, and 3 exhibit large dispersions in downrange. These dispersions give a misleading impression of the achieved performances because the PoI map does not display the PoI concentrations. Analysis of the PoI map in parallel with the cumulative distribution graphic (Fig. 9) is therefore required. The cumulative distributions show that more than 60% of the misses are close to the target. Therefore, only the less than 40% remaining misses contribute to the large dispersions observed in Fig. 11. With an analysis of the PoIs and their displacement between the unguided and guided concepts, the large misses of the guided fuzes can be traced back to conventional PoIs located outside the guided fuze footprints. Also, because of the prioritization effect of the guidance law, Concepts 1 and 2 still have some residual crossrange misses.

Conclusion

This paper studied four canards-based course correction fuzes. Simulations of these concepts with the developed guidance and control algorithms demonstrated that the four concepts are able to drastically improve the precision of a spin-stabilized projectile. Furthermore, the observed miss distributions are coherent with the footprints and guidance law behavior. Under the proposed guidance and control algorithms, a concept able to control the longitudinal

acceleration, like the proposed regulated roll angle ring equipped with four actuated canards having different deflection limits, provides precision significantly better than that offered by concepts using only the lift force as an aerodynamic control force. For the latter type of concepts, the axes decoupling provides an improvement. The miss distribution pattern is similar for all tested quadrant elevations and the precision is slightly better. Even if, among the proposed concepts and with the proposed algorithms, the concept with fixed canards provides the worst precision, the improvement, in comparison with an unguided fuze, is significant enough to identify it as a mechanically simple and efficient solution.

References

Bybee, T. (2010). "Precision guidance kit." *45th Annual NDIA Gun and Missile Systems Conf. & Exhibition*, National Defense Industrial Association (NDIA), Arlington, VA.

Calise, A. J., and El-Shirbiny, H. A. (2001). "An analysis of aerodynamic control for direct fire spinning projectile." *AIAA Guidance, Navigation and Control Conf. and Exhibit*, American Institute of Aeronautics and Astronautics, Reston, VA.

Costello, L. D., and Peterson, A. A. (2000). "Linear theory of a dual-spin projectile." *Rep. No. ARL-CR-448*, U.S. Army Research Laboratory, Aberdeen Proving Ground, MD.

Fairfax, L. D., and Fresconi, F. E. (2012). "Position estimation for projectile using low-cost sensor and flight dynamics." *Rep. No. ARL-TR-5994*, U.S. Army Research Laboratory, Aberdeen Proving Ground, MD.

Fresconi, F. (2011). "Guidance and control of a fin-stabilized projectile based on flight dynamics with reduced sensor and actuator requirements." *Rep. No. ARL-TR-5458*, U.S. Army Research Laboratory, Aberdeen Proving Ground, MD.

Fresconi, F., Celmins, I., Silton, S., and Costello, M. (2015). "High maneuverability projectile flight using low cost components." *Aerosp. Sci. Technol.*, 41, 175–188.

Fresconi, F., Cooper, G., and Costello, M. (2011). "Practical assessment of real-time impact point estimators for smart weapons." *J. Aerosp. Eng.*, 10.1061/(ASCE)AS.1943-5525.0000044, 1–11.

Gagnon, E., and Lauzon, M. (2008). "Course correction fuze concept analysis for in-service 155 mm spin-stabilized gunnery projectile." *AIAA Guidance, Navigation and Control Conf. and Exhibit*, American Institute of Aeronautics and Astronautics, Reston, VA.

Gagnon, E., Pomerleau, A., and Desbiens, A. (1998). "Simplified, ideal or inverted decoupling?" *ISA Trans.*, 37(4), 265–276.

Grignon, C., Cayzac, R., and Heddadj, S. (2007). "Improvement of artillery projectile accuracy." *23rd Int. Symp. on Ballistics*, International Ballistics Society, San Antonio, TX.

Hillstrom, T., and Osborne, P. (2005). "United defense course correcting fuze for the projectile guidance kit program." *49th NDIA Annual Fuze Conf.*, National Defense Industrial Association, Arlington, VA.

Hollis, M. S. L., and Brandon, F. J. (1999). "Design and analysis of a fuze-configurable range correction device for an artillery projectile." *Rep. No. ARL-TR-2074*, U.S. Army Research Laboratory, Aberdeen Proving Ground, MD.

Kautzsch, K. B., and Reusch, O. (2003). "Precision enhancement build on a multi functional fuze for 155 mm artillery munition." *47th NDIA Annual Fuze Conf.*, National Defense Industrial Association, Arlington, VA.

Lieske, R. F., and Reiter, M. L. (1966). "Equations of motion for a modified point mass trajectory." *Rep. No. BRL R 1314*, Ballistic Research Laboratories, Aberdeen Proving Ground, MD.

Lloyd, K. H., and Brown, D. P. (1979). "Instability of spinning projectiles during terminal guidance." *J. Guidance Control Dyn.*, 2(1), 65–70.

McCoy, R. L. (2012). *Modern exterior ballistics*, Schiffer, Atglen, PA.

Ollerenshaw, D., and Costello, M. (2008). "Simplified projectile swerve solution for general control inputs." *J. Guidance Control Dyn.*, 31(5), 1259–1265.

Park, W., Ryoo, C.-K., Kim, B. S., Kim, Y., and Kim, J. (2011). "A new practical guidance law for a guided projectile." *AIAA Guidance, Navigation and Control Conf.*, American Institute of Aeronautics and Astronautics, Reston, VA.

PRODAS version 3.5.3 [Computer software]. ArrowTech Associates, South Burlington, VT.

Reagan, F. J., and Smith, J. (1975). "Aeroballistics of a terminally corrected spinning projectile." *J. Spacecraft Rockets*, 12(12), 733–738.

Robinson, J. W. C., and Strömbäck, P. (2013). "Perturbation based guidance for a generic 2D course correcting fuze." *AIAA Guidance, Navigation, and Control Conf.*, American Institute of Aeronautics and Astronautics, Reston, VA.

Rogers, J., and Costello, M. (2010). "Design of a roll-stabilized mortar projectile with reciprocating canards." *J. Guidance Control Dyn.*, 33(4), 1026–1034.

Rosema, C., Doyle, J., Auman, L., and Underwood, M. (2011). "Missile datcom, user's manual—2011 revision." *Rep. No. AFRL-RB-WP-TR-2011-3071*, U.S. Army Aviation & Missile Research, Redstone Arsenal, AL.

Teofilatto, P., and De Pasquale, E. (1998). "A fast guidance algorithm for an autonomous navigation system." *Planet. Space Sci.*, 46(11-12), 1627–1632.

Theodoulis, S., Gassmann, V., Brunner, T., and Wernert, P. (2013a). "Fixed structure robust control design for the 155 mm canard-guided projectile roll-channel autopilot." *Proc., 21st Mediterranean Conf. on Control Automation*, IEEE, Piscataway, NJ.

Theodoulis, S., Gassmann, V., Brunner, T., and Wernert, P. (2013b). "Robust bank-to-turn autopilot design for a class of 155 mm spin-stabilized canard-guided projectiles." *AIAA Atmospheric Flight Mechanics Conf.*, American Institute of Aeronautics and Astronautics, Reston, VA.

Theodoulis, S., Sve, F., and Wernert, P. (2015). "Robust gain-scheduled autopilot design for spin-stabilized projectiles with a course-correction fuze." *Aerosp. Sci. Technol.*, 42, 477–489.

Welch, G., and Bishop, G. (2006). "An introduction to the Kalman filter." *Rep. No. TR-95-041*, Univ. of North Carolina at Chapel Hill, Chapel Hill, NC.

Wernert, P., Leopold, F., Bidino, D., Juncker, J., Lehmann, L., Bär, K., and Reindler, A. (2008). "Wind tunnel tests and open-loop trajectory simulations for a 155 mm canards guided spin stabilized projectile." *AIAA Atmospheric Flight Mechanics Conf. and Exhibit*, American Institute of Aeronautics and Astronautics, Reston, VA.

Wernert, P., Theodoulis, S., and Morel, Y. (2010). "Flight dynamics properties of 155 mm spin-stabilized projectiles analyzed in different body frames." *AIAA Atmospheric Flight Mechanics Conf.*, American Institute of Aeronautics and Astronautics, Reston, VA.